

Unsupervised Unfolded rPCA (U²-rPCA): Deep Interpretable Clutter Filtering for Ultrasound Microvascular Imaging

Huaying Li, Liansheng Wang, *Member, IEEE*, Yinran Chen, *Member, IEEE*

Abstract—High-sensitivity clutter filtering is a fundamental step in ultrasound microvascular imaging. Singular value decomposition (SVD) and robust principal component analysis (rPCA) are the main clutter filtering strategies. However, both strategies are limited in feature modeling and tissue-blood flow separation for high-quality microvascular imaging. Recently, deep learning-based clutter filtering has shown potential in more thoroughly separating tissue and blood flow signals. However, the existing supervised filters face the challenges of interpretability and lack of *in-vitro* and *in-vivo* ground truths. While the interpretability issue can be addressed by algorithm deep unfolding, the training ground truth remains unsolved. To this end, this paper proposes an unsupervised unfolded rPCA (U²-rPCA) method that preserves mathematical interpretability and is insusceptible to learning labels. Specifically, U²-rPCA is unfolded from an iteratively reweighted least squares (IRLS) rPCA baseline with intrinsic low-rank and sparse regularization. A sparse-enhancement unit is added to the network to strengthen its capability to capture the sparse micro-flow signals. U²-rPCA is like an adaptive filter that is trained with part of the image sequence and then used for the following frames. Experimental validations on a *in-silico* dataset and public *in-vivo* datasets demonstrated the outperformance of U²-rPCA when compared with the SVD-based method, the rPCA baseline, and another deep learning-based filter. Particularly, the proposed method improved the contrast-to-noise ratio (CNR) of the power Doppler image by 2 dB to 10 dB when compared with other methods. Furthermore, the effectiveness of the building modules of U²-rPCA was validated through ablation studies.

Index Terms—Clutter filtering, deep unfolding, interpretability, robust PCA, ultrasound microvascular imaging, unsupervised learning.

I. INTRODUCTION

Ultrasound is a fundamental medical imaging modality due to its real-time, radiation-free, and cost-effective advantages. Blood flow imaging is one of the most featured functions in ultrasound. Since microvasculature and hemodynamics are important indicators for the diagnosis and assessment of many diseases, ultrasound microvascular imaging, including ultrasound localization microscopy (ULM), has emerged as a powerful method for visualizing and quantifying microvasculature in various laboratory and clinical applications [1], [2].

(Corresponding authors: Liansheng Wang and Yinran Chen).

H. Li and Y. Chen are with the Fujian Key Laboratory of Sensing and Computing for Smart City, School of Informatics, Xiamen University, Xiamen 361005, China (e-mail: lihuaying@stu.xmu.edu.cn, yinran_chen@xmu.edu.cn).

L. Wang is with the Department of Computer Science and Technology, School of Informatics, and the National Institute for Data Science in Health and Medicine, Xiamen University, Xiamen 361005, China (e-mail: lswang@xmu.edu.cn).

Ultrafast beamforming, spatiotemporal clutter filtering, and denoising technologies facilitate the developments of ultrasound microvascular imaging [3]–[5]. Clutter filtering is the key to discriminating microvessels and tissues from the raw ultrasonic sequence. The success of clutter filtering highly relies on feature modeling of the tissue and blood flow signals. Currently, microvascular imaging employs singular value decomposition (SVD) and robust principal component analysis (rPCA) to leverage spatial and temporal coherence of tissue and blood flow signals for high-sensitivity filtering. SVD-based methods assume that tissue and blood flow occupy different subspaces when the raw ultrasonic sequence is stacked into a Casorati matrix. The key step is to threshold the singular values of tissue and noise and recover the subspace of blood flow [4]. SVD has been the most popular approach for microvascular imaging. However, the performance of SVD clutter filtering is determined by elaborately fine-tuning the singular values of blood flow. rPCA-based methods leverage the low rankness of tissue and the sparsity of blood flow in the raw ultrasonic sequence and transfer clutter filtering into a problem of low-rank and sparse decomposition [6]. Since the original form of rPCA is NP-hard, various relaxation strategies for the low-rankness and sparsity terms have been proposed. Nevertheless, the rPCA-based methods are sensitive to the hyperparameters, which also require elaborate fine-tuning. In addition, the time efficiency is limited by the iterative calculations for convergence.

SVD and rPCA-based methods employ algorithmic assumptions to separate tissue and blood flow signals. However, real imaging scenarios with complex acoustic clutter and noise can violate elegant mathematical formulations. In recent years, deep learning has emerged as a data-driven tool that can better capture data complexity and thus improve microvascular clutter filtering [7]–[9]. General deep learning-based clutter filters are constructed from building blocks such as convolutional neural networks (CNN), resulting in the lack of interpretability. Alternatively, the iterative algorithms can be unfolded into successive interpretable layers [10]. Deep unfolding, or deep unrolling, offers promise in providing a concrete connection between iterative algorithms and deep neural networks [11], [12], which has attracted enormous attention from the research fields such as CT [13], MR [14], [15], ultrasound [16], [17], and other computer vision tasks [18]. In deep-unfolded clutter filtering, training data become critical since the current networks are trained in a supervised manner (see Table I). Although supervised deep clutter filters are more likely to learn

TABLE I
DEEP LEARNING-BASED CLUTTER FILTERING METHODS FOR ULTRASOUND MICROVASCULAR IMAGING

Category	Authors	Model	Training Approach	Training Data
Unfolded	Pustovalov <i>et al</i> [32].	DRPCANet	Supervised	<i>In-silico</i>
	Solomon <i>et al</i> [27].	CORONA	Supervised	<i>In-silico</i> + <i>In-vivo</i> (rPCA)
Conventional	Shih <i>et al</i> [28].	Autoencoder	Supervised	<i>In-silico</i>
	Brown <i>et al</i> [29].	3DCNN	Supervised	<i>In-vitro</i> (SVD) + <i>In-vivo</i> (SVD)
	Wang <i>et al</i> [7].	LSTM	Supervised	<i>In-vivo</i> (SVD)
	Ehrenstein <i>et al</i> [8].	RA-DR ² Net	Supervised	<i>In-silico</i>
	Minhaz <i>et al</i> [31].	2D U-Net	Supervised	<i>In-vivo</i> (SVD)
	Ianni <i>et al</i> [30].	3D-Res-UNet	Supervised	<i>In-vivo</i> (SVD)

more implicit feature differences between tissue and blood flow, the ground truths of *in-vitro* and *in-vivo* tissue and blood flow signals are technically inaccessible. As a result, either *in-silico* simulations or *in-vitro* and *in-vivo* datasets obtained by conventional methods have to be used for training. The simulation strategy is preferred to mimic the microvasculature characteristics, such as morphology, hemodynamics, and coupling between tissue and vessels. However, most present simulations employ simple convolutions between random-moving scatterers and a point spread function (PSF). In contrast, the *in-vitro* and *in-vivo* datasets highly rely on the effectiveness of conventional clutter filtering methods, e.g., SVD and rPCA, which still face limitations in complex imaging applications.

Deep unfolded clutter filtering shows potential in high-quality ultrasound microvascular imaging. However, the quality of training data limits the performance of supervised filters. Since rPCA is an unsupervised procedure that explores the intrinsic low rankness of tissue and sparsity of blood flow, this paper proposes an Unsupervised Unfolded rPCA (U²-rPCA) method that can (i) better separate tissue and blood flow via interpretable deep learning and (ii) be free of training ground truths. The technical contributions of this paper are clarified as follows.

- We construct the U²-rPCA clutter filter based on an Iteratively Reweighted Least Squares rPCA (IRLS-rPCA) baseline. All the terms of IRLS-rPCA are formulated with the Frobenius norm so that they are directly unfolded and transferred to the equivalent MSE loss functions with intrinsic low-rank and sparse regularization. As a result, the network is trained in an unsupervised manner without losing interpretability.
- We transfer the predefined weights and penalty coefficients of IRLS-rPCA into learnable matrices and parameters to increase U²-rPCA's ability in learning and distinguishing the features of tissue and blood flow. Additionally, no extra effort should be paid to fine-tune the penalty coefficients, which originally played an important role in the rPCA model.
- We enhance the performance of U²-rPCA in resolving the micro blood flow signals by adding a sparse-enhancement unit (SEU) to the unfolded layers. The unit includes a dual-frame U-Net module that assists the network in better learning the sparse spatiotemporal coherence and improving the effectiveness of blood flow extraction.

We evaluated U²-rPCA in a *in-silico* dataset and the public

PALA *in-vivo* datasets including a rat kidney and a mouse tumor. Extensive experiments demonstrated the effectiveness and interpretability of U²-rPCA and its outperformance when compared with other clutter filtering methods.

II. RELATED WORK

SVD-based clutter filtering requires three main steps: decomposing the raw ultrasonic sequence, thresholding the singular values, and recovering blood flow signals from its subspace. Following this procedure, Demeⁿe *et al.* [4] first introduced SVD to ultrafast power Doppler imaging (uPDI). For the two-cutoff thresholding, Song *et al.* [19] estimated the cutoffs using local data statistics of singular values and vectors. Baranger *et al.* [20] recommended a cutoff estimator based on the spatial similarity matrix. This method was then improved for fast realization through a sum-table approach [21]. The two-cutoff assumption is not rigorous since the subspaces of tissue, blood flow, and noise are not independent of each other. Each singular vector may contain the contributions from different components. Waraich *et al.* [22] employed K-means to cluster the singular ranks of blood flow for clutter filtering. In our previous work [23], [24], we proposed to use competitive swarm optimization (CSO) to identify the proportion of blood flow in each singular value for improved uPDI.

rPCA-based clutter filtering decomposes the low-rank tissue and sparse blood flow via iterative calculations until convergence. Bayat and Fatemi *et al.* [6] proposed to use nuclear norm and frequency-domain l_1 -norm to model tissue signals and blood flow signals, respectively. Xu *et al.* [25] used conventional l_1 -norm for the sparse blood flow signals. This group also adopted the Cauchy norm to replace the nuclear norm and the l_1 -norm for tissue and blood flow signals [26]. Solomon *et al.* [27] proposed the mixed $l_{1,2}$ -norm to strengthen the sparsity of blood flow signals. They also used the rPCA filtering results to supervise the training of a corresponding unfolding network.

As illustrated in Table I, deep learning-based clutter filtering can be divided into conventional and unfolding-based models. The conventional models construct the networks using blocks such as CNN and long-short-term memory (LSTM). Shih *et al.* [28] proposed a convolutional autoencoder for clutter suppression and power Doppler reconstruction. Brown *et al.* [29] applied 3DCNN to spatiotemporal filter in fast super-resolution ultrasound imaging. Ianni *et al.* [30] proposed a 3D-Res-UNet

to learn the power Doppler reconstruction function from sparse sequences in functional ultrasound imaging. Other classical deep neural modules, such as 2D U-Net [31], LSTM [7], and deep residual reconstruction [8] are also used for microvascular clutter filtering. CORONA [27] is a representative of deep unfolded clutter filtering methods. It unfolds a rPCA model including a nuclear norm and a mixed $l_{1,2}$ -norm into multiple layers and trains the network with *in-silico* simulations and *in-vivo* data obtained from the rPCA baseline. The original nuclear norm and $l_{1,2}$ -norm are replaced with a mean square error (MSE) loss to measure the discrepancy between the network's outputs and the training data. Pustovalov *et al.* [32] unfolded a deconvolutional rPCA model into a DRPCANet to improve spatial resolution in the microvascular flow estimation. Table I clarifies that the abovementioned methods were trained in a supervised manner. As a result, the training data not only requires extra time and effort for collection but also significantly affects the performance of the filters.

III. METHODS

A. Problem Formulation

In ultrasound microvascular imaging, a raw sequence $\mathbf{D} \in \mathbb{C}^{N_z, N_x, N_t}$ is acquired from ultrafast plane wave beamforming. Here, N_x and N_z are the number of pixels in the lateral and axial dimensions, respectively. N_t is the number of frames. For clutter filtering, the raw sequence \mathbf{D} is first reshaped into a Casorati matrix $\mathbf{D} \in \mathbb{C}^{N_s, N_t}$ ($N_s = N_z \times N_x$), where each column of \mathbf{D} corresponds to one frame that is vectorized into a column vector. The fundamental assumption is straightforward: the raw sequence is the summation of tissue signals \mathbf{T} , blood flow signals \mathbf{B} , and additive noise \mathbf{N} :

$$\mathbf{D} = \mathbf{T} + \mathbf{B} + \mathbf{N} \quad (1)$$

In the Casorati form, tissue signals \mathbf{T} are assumed to be low-rank because they are static or moving slowly in contrast to the embedded microvessels. The blood flow signals \mathbf{B} are dynamic within the microvascular networks, which are assumed to be spatially sparse. In addition, the spatial distribution of the microvessels is stable during the short and ultrafast acquisition. Therefore, the classical rPCA-based clutter filtering aims at solving the following low-rank and sparse decomposition:

$$\min_{\mathbf{T}, \mathbf{B}} \text{rank}(\mathbf{T}) + \lambda \|\mathbf{B}\|_0 \quad \text{s.t. } \mathbf{T} + \mathbf{B} = \mathbf{D} \quad (2)$$

where $\text{rank}(\cdot)$ computes the rank of a given matrix. $\|\cdot\|_0$ denotes the number of non-zero elements in a given vector or matrix. Since solving Eq. (2) is NP-hard, several strategies have been proposed to relax $\text{rank}(\mathbf{T})$ and $\|\mathbf{B}\|_0$ into solvable terms [33], [34], among which the nuclear norm for tissue and the l_1 -norm for blood flow are commonly used:

$$\min_{\mathbf{T}, \mathbf{B}} \|\mathbf{T}\|_* + \lambda \|\mathbf{B}\|_1 \quad \text{s.t. } \mathbf{T} + \mathbf{B} = \mathbf{D} \quad (3)$$

where $\|\cdot\|_*$ computes the summation of the singular values of a given matrix, and $\|\cdot\|_1$ computes the absolute sum of all the elements of a given vector or matrix. According to [35], [36], the nuclear norm term is iteratively optimized by singular value thresholding, whereas the l_1 -norm term is updated by

Algorithm 1 IRLS-rPCA

Input: \mathbf{D} , d , λ_c , λ_b , and ϵ

Output: blood flow signals \mathbf{B}

Initialization:

$$\mathbf{U}_0 = \text{orth}(\mathbf{D}(:, 1:d))$$

$$\mathbf{V}_0 = \mathbf{D}^* \mathbf{U}_0$$

$$\mathbf{B}_0 = \text{zeros}(N_s, N_t) + j\text{zeros}(N_s, N_t)$$

$$k = 1$$

while $k \leq$ (maximum iteration) **do**

 Update $\mathbf{W}_{b,k}$ using Eq.(7)

 Update \mathbf{B}_k using Eq.(9)

 Update \mathbf{V}_k using Eq.(10)

 Update \mathbf{U}_k using Eq.(11)

 Update $\mathbf{W}_{c,k}$ using Eq.(6)

if $\left(\frac{\|\mathbf{B}_k + \mathbf{T}_k - \mathbf{B}_{k-1} - \mathbf{T}_{k-1}\|_F^2}{\|\mathbf{B}_{k-1} + \mathbf{T}_{k-1}\|_F^2} \right) < \epsilon$ **then**

break

end if

end while

return $\mathbf{B} \leftarrow \mathbf{B}_k$

soft thresholding. However, singular value thresholding is time-consuming because SVD is needed for each iteration. More importantly, directly setting the nuclear norm and l_1 -norm as the loss function for U^2 -rPCA results in difficulties in training for convergence.

B. Iteratively Reweighted Least Squares (IRLS) rPCA

To properly unfold the rPCA clutter filter into an unsupervised network, new relaxations to the nuclear norm and the l_1 -norm are needed. Fortunately, Daubechies *et al.* [37] proposed and proved that a solution x^* of l_1 -norm coincides with a unique sparse-recovery solution x of an iteratively reweighted least squares (IRLS) sparse minimization $\|\mathbf{x} \odot \mathbf{w}^{\frac{1}{2}}\|_2$, where $\mathbf{w}_j = |\mathbf{x}_j^*|^{-1}$ and \odot denotes Hadamard product. Motivated by [37], Giampouras *et al.* [38] extended IRLS to low-rank minimization. They proposed and proved that the nuclear norm $\|\mathbf{X}\|_*$ has a tight upper bound $\left(\|\mathbf{U}\mathbf{W}_c^{\frac{1}{2}}\|_F + \|\mathbf{V}\mathbf{W}_c^{\frac{1}{2}}\|_F \right)$, where $\mathbf{X} = \mathbf{U}\mathbf{V}^*$ and \mathbf{W} is the corresponding weights defined as $\mathbf{W}_c = \text{diag} \left(\left(\|\mathbf{U}(:, 1)\|_2^2 + \|\mathbf{V}(:, 1)\|_2^2 + \epsilon \right)^{\frac{\rho}{2}-1}, \dots, \left(\|\mathbf{U}(:, d)\|_2^2 + \|\mathbf{V}(:, d)\|_2^2 + \epsilon \right)^{\frac{\rho}{2}-1} \right)$, where $0 < \rho \leq 1$. $\|\cdot\|_F$ denotes the matrix Frobenius norm. Therefore, the low-rank \mathbf{T} can be equivalently formulated as $\mathbf{T} = \mathbf{U}\mathbf{V}^*$, where $\mathbf{U} \in \mathbb{C}^{N_s, d}$ is the basis that spans the subspace of \mathbf{T} . $\mathbf{V} \in \mathbb{C}^{N_t, d}$ acts as the coordinate coefficients of \mathbf{T} under \mathbf{U} . As a result, Eq. (1) is rewritten as

$$\mathbf{D} = \mathbf{U}\mathbf{V}^* + \mathbf{B} + \mathbf{N} \quad (4)$$

where the superscript $*$ means conjugate transpose. d is the inner dimension of the matrix \mathbf{T} with $r < d \ll \min(N_s, N_t)$, where r is the true rank of \mathbf{T} . The inner dimension d is larger than r because the true rank of tissue signals is not exactly known. The tissue basis should be designed with redundancy

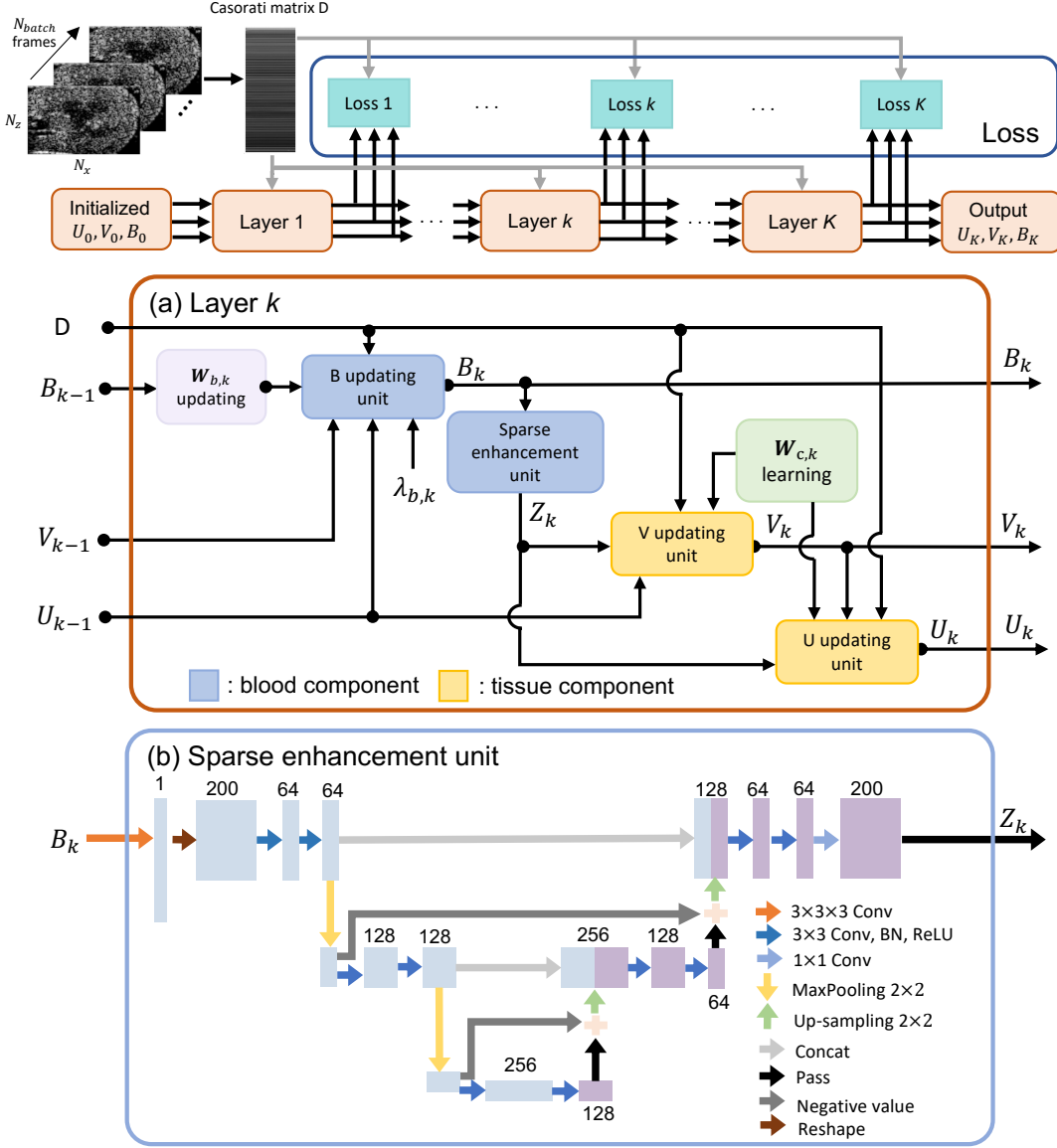


Fig. 1. The framework of the U^2 -rPCA clutter filter. (a) is the realization in the k -th layer. (b) is the architecture of the sparse-enhancement unit.

to deal with the complex clutter and noise. With the IRLS approach, the baseline of U^2 -rPCA is formulated as [39]

$$\min_{\substack{\mathbf{U}, \mathbf{V}, \mathbf{B}, \\ \mathbf{W}_c, \mathbf{W}_b}} \lambda_c \left(\|\mathbf{U}\mathbf{W}_c^{\frac{1}{2}}\|_F^2 + \|\mathbf{V}\mathbf{W}_c^{\frac{1}{2}}\|_F^2 \right) + \lambda_b \|\mathbf{B} \odot \mathbf{W}_b^{\frac{1}{2}}\|_F^2 \quad (5)$$

s.t. $\mathbf{U}\mathbf{V}^* + \mathbf{B} = \mathbf{D}$

where λ_c and λ_b are the penalty coefficients for the low-rank and the sparse regularization, respectively. $\mathbf{W}_c \in \mathbb{R}^{d,d}$ are the weights for the low-rank term:

$$\mathbf{W}_c = \text{diag} \left(\left(\|\mathbf{U}(:, 1)\|_2^2 + \|\mathbf{V}(:, 1)\|_2^2 + \epsilon \right)^{-\frac{1}{2}}, \dots, \left(\|\mathbf{U}(:, d)\|_2^2 + \|\mathbf{V}(:, d)\|_2^2 + \epsilon \right)^{-\frac{1}{2}} \right), \quad (6)$$

where $\text{diag}(\cdot)$ transfers a given vector into a diagonal matrix. ϵ is a small positive constant to avoid singularity. According

to [39] and [37], each element of the weight matrix $\mathbf{W}_b \in \mathbb{R}^{N_s, N_t}$ for the sparse term is defined as

$$\mathbf{W}_b(i, j) = (\mathbf{B}(i, j)^2 + \epsilon)^{-\frac{1}{2}} \quad (7)$$

The constraint of Eq. (5) can be substituted with a data-consistency term, resulting in the following quadratic minimization problem:

$$\min_{\mathbf{U}, \mathbf{V}, \mathbf{B}, \mathbf{W}_c, \mathbf{W}_b} \frac{1}{2} \|\mathbf{D} - \mathbf{U}\mathbf{V}^* - \mathbf{B}\|_F^2 + \lambda_c \left(\|\mathbf{U}\mathbf{W}_c^{\frac{1}{2}}\|_F^2 + \|\mathbf{V}\mathbf{W}_c^{\frac{1}{2}}\|_F^2 \right) + \lambda_b \|\mathbf{B} \odot \mathbf{W}_b^{\frac{1}{2}}\|_F^2 \quad (8)$$

Eq. (8) is solved by alternately updating \mathbf{B}_k , \mathbf{U}_k , \mathbf{V}_k , and the weight matrices until convergence. Here k denotes the index of iterations. The specific updating formulations are clarified as follows:

$$\mathbf{B}_k = (\mathbf{D} - \mathbf{U}_{k-1} \mathbf{V}_{k-1}^*) \oslash (1 + 2\lambda_b \mathbf{W}_{b,k}) \quad (9)$$

$$\mathbf{V}_k = (\mathbf{D} - \mathbf{B}_k)^* \mathbf{U}_{k-1} (\mathbf{U}_{k-1}^* \mathbf{U}_{k-1} + 2\lambda_c \mathbf{W}_{c,k-1})^{-1} \quad (10)$$

$$\mathbf{U}_k = (\mathbf{D} - \mathbf{B}_k)^* \mathbf{V}_k (\mathbf{V}_k^* \mathbf{V}_k + 2\lambda_c \mathbf{W}_{c,k-1})^{-1} \quad (11)$$

where \oslash denotes element-wise division. In each iteration, $\mathbf{W}_{b,k}$ is updated according Eq. (7) before \mathbf{B}_k . $\mathbf{W}_{c,k}$ is updated using Eq. (6) following \mathbf{U}_k . Algorithm 1 summarizes the realizations of IRLS-rPCA clutter filtering. As illustrated in Eq. (8), all the terms are formulated with the Frobenius norm, which is mathematically equivalent to the l_2 -norm, or more specifically, the MSE loss function for deep learning. The good properties of continuity and differentiability of the Frobenius norm can facilitate the training of U²-rPCA in an unsupervised manner.

C. U²-rPCA Architecture

Fig. 1 shows the architecture of U²-rPCA. The baseline IRLS-rPCA is unfolded into a succession of K layers (Fig. 1(a)). The number of layers, K , is like the number of iterations for convergence in Algorithm 1. Therefore, this hyperparameter is task-driven and should be predefined according to different imaging scenarios. The calculations in each layer are similar to a loop in Algorithm 1. Specifically, in the k -th layer, the blood flow \mathbf{B} , the tissue basis \mathbf{U} , and the tissue coordinate coefficients \mathbf{V} are updated based on the outputs of the $(k-1)$ -th layer and put forward to the $(k+1)$ -th layer. \mathbf{W}_b is determined, whereas \mathbf{W}_c is set as learnable. Furthermore, a sparse-enhancement unit (SEU) right after the update of \mathbf{B} is added to each layer.

1) **B Updating Unit:** As illustrated in Fig. 1(a), this unit first takes \mathbf{B}_{k-1} to update $\mathbf{W}_{b,k}$ according to Eq. (7). Then, \mathbf{U}_{k-1} and \mathbf{V}_{k-1} of the $(k-1)$ -th layer, $\mathbf{W}_{b,k}$ of this layer, and the raw sequence \mathbf{D} are put together to update \mathbf{B}_k . Similar to Eq. (9), the formulation of the B updating unit is

$$\mathbf{B}_k = (\mathbf{D} - \mathbf{U}_{k-1} \mathbf{V}_{k-1}^*) \oslash (1 + 2\lambda_{b,k} \mathbf{W}_{b,k}) \quad (12)$$

The difference between Eq. (12) and Eq. (9) is that the penalty coefficient $\lambda_{b,k}$ becomes a learnable parameter. It should be noted that $\mathbf{W}_{b,k}$ is determined according to Eq. (7) rather than being set as learnable parameters. This is because Eq. (7) is a sparsity constraint with rigorous mathematical proofs. The deterministic $\mathbf{W}_{b,k}$ helps the U²-rPCA network maintain its intrinsic sparse regularization.

2) **Sparse Enhancement Unit (SEU):** The unsupervised manner of U²-rPCA means that the network cannot learn the feature differences between tissue and blood flow from referenced or ground-truth datasets. The consequence is that the performance of the unfolded version may be very close to that of the IRLS-rPCA baseline. To strengthen the capability of U²-rPCA in extracting the features of sparse blood flow signals in the spatial domain, we added a plug-in SEU module after the B updating unit. SEU is composed of a dual-frame U-Net, which has been applied to recover high-frequency edges in sparse-view CT [40] and unsupervised video foreground separation [41]. Fig. 1(b) shows that the dual-frame U-Net is a symmetrical U-shaped network. In this module, the features

obtained by upsampling in the decoder will be subtracted from the features downsampled in the encoder at the same scales. As a result, more refined sparse features of the blood flow can be extracted and fed into the following units. The output of SEU \mathbf{Z}_k is formulated as

$$\mathbf{Z}_k = \text{SEU}_{\theta,k}(\mathbf{B}_k) \quad (13)$$

where $\text{SEU}(\cdot)$ denotes the operation of the SEU module. θ, k are the learnable parameters of the dual-frame U-Net in the k -th layer. As a plug-in module, the inputs and outputs of this module are the features representing the sparse blood flow signals with identical dimensions. Either the inputs or the outputs of this module can be passed to the following unit. It should be noted that the dual-frame U-Net is realized in a complex network because the entire workflow of U²-rPCA is implemented on the complex data.

3) **V and U Updating Units:** The unfolding operation turns λ_c and \mathbf{W}_c in Eq. (8) into learnable parameters. Notably, λ_c can be integrated into the learning of \mathbf{W}_c . The advantage is that U²-rPCA becomes free of λ_c , which originally requires extensive fine-tuning for the success of the conventional rPCA-based methods. With this improvement, the V updating unit takes the output of the SEU \mathbf{Z}_k , the previous tissue basis \mathbf{U}_{k-1} , and the raw sequence \mathbf{D} as input. The updated \mathbf{V}_k is defined as

$$\mathbf{V}_k = (\mathbf{D} - \mathbf{Z}_k)^* \mathbf{U}_{k-1} (\mathbf{U}_{k-1}^* \mathbf{U}_{k-1} + \mathbf{W}_{c,k})^{-1} \quad (14)$$

Similarly, \mathbf{V}_k and other necessary components are fed into the following U updating unit for the update of \mathbf{U}_k :

$$\mathbf{U}_k = (\mathbf{D} - \mathbf{Z}_k)^* \mathbf{V}_k (\mathbf{V}_k^* \mathbf{V}_k + \mathbf{W}_{c,k})^{-1} \quad (15)$$

Compared to the IRLS-rPCA baseline, the only hyperparameter in this unit is the inner dimension of the tissue basis, d . This hyperparameter limits the dimensions of \mathbf{U}_k and \mathbf{V}_k so that U²-rPCA can maintain its intrinsic low-rank regularization to the tissue signals.

D. Loss Function

Eq. (8) shows that IRLS-rPCA uses the Frobenius norm to model all the terms to be optimized. The definition of the Frobenius norm for a matrix is mathematically equivalent to the l_2 -norm for a vector. Therefore, it is straightforward and rational to employ MSE as the loss function to train the network. Furthermore, we refer to the deep supervised scheme and apply unsupervised MSE loss functions to the outputs of all the layers. The final loss function of U²-rPCA is defined as

$$\text{Loss} = \frac{1}{K} \sum_{k=1}^K \|\mathbf{D} - \mathbf{B}_k - \mathbf{U}_k \mathbf{V}_k^*\|_F^2 \quad (16)$$

where K is the number of layers. It is worth mentioning that the low-rankness of $\mathbf{U}_k \mathbf{V}_k^*$ and the sparsity of \mathbf{B}_k can be promoted during the layer-wise alternate updates. Therefore, there is no need to add extra low-rank and sparse regularization to the loss function.

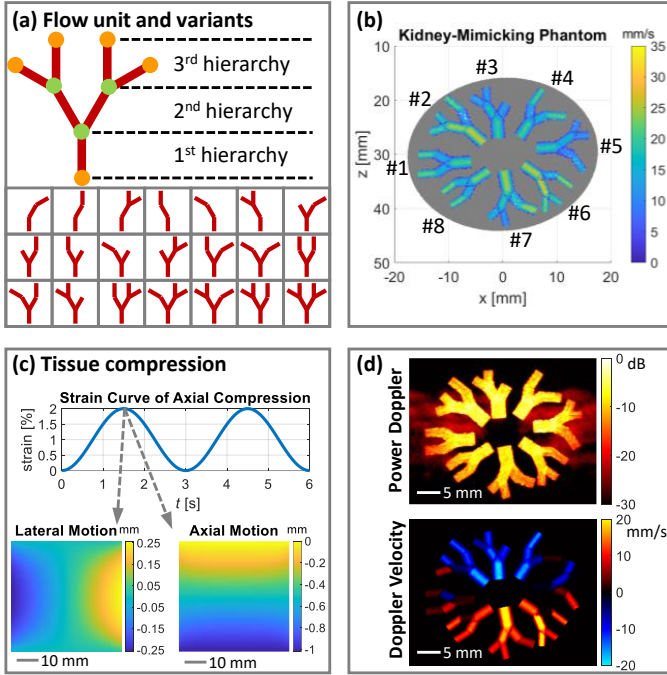


Fig. 2. Configurations of the *in-silico* kidney-mimicking phantom. (a) illustrates the basic flow unit and its variants. (b) is the geometry of this phantom and the velocities in the flow units. (c) shows the finite-element-analysis (FEA)-based axial-compression strain curve and the lateral and axial displacements applied to the phantom. (d) presents the ground-truth power Doppler image and Doppler velocity image

TABLE II
SIMULATION PARAMETERS OF THE FLOW UNIT

Parameter	Hierarchy	Range of value
L	1	$3.5 + [-0.35, 0.35]$ mm
	2	$3.5 + [-0.35, 0.35]$ mm
	3	$3.5 + [-0.35, 0.35]$ mm
S	1	$[-10^\circ, 10^\circ]$
	2	$\pm 30^\circ \pm [-2^\circ, 2^\circ]$
	3	$60^\circ \pm [-3^\circ, 3^\circ]$ and $[-3^\circ, 3^\circ]$
R	1	$1.25 \pm [-0.125, 0.125]$ mm
	2	Depends on R_1
	3	Depends on R_2
V_{max}	1	$[20, 30]$ mm/s
	2	Depends on V_{max1}
	3	Depends on V_{max1} and V_{max2}

IV. EXPERIMENTAL SETTINGS

A. In-Silico Experiments

Fig. 2 illustrates the simulation configurations. Inspired by the kidney microvasculature, we constructed a kidney-mimicking phantom that comprises several multi-hierarchy flow units distributing radially in an oval-like region (see Fig. 2(b)). The complete flow unit is composed of three hierarchies, each of which includes 1, 2, and 4 sub-branches, respectively (see Fig. 2(a)). Fig. 2(a) also lists all the sub-structures of the unit that contain three hierarchies. Eight sub-structures were randomly selected with repeatability to form the numerical kidney phantom in Fig. 2(b).

Randomness is also applied to the parameters of the flow units. Table II shows that the lengths (L_1 , L_2 , and L_3) and steering angles (S_1 , S_2 , and S_3) of all the sub-branches, and the radius of the first sub-branch (R_1) are randomly specified in the given ranges. The radii of the following sub-branches (R_2 and R_3) are determined accordingly to maintain the smoothness of the unit geometry. The maximal velocity in the first sub-branch of each unit is randomly set between 20 mm/s and 30 mm/s. The fluid dynamics of the other sub-branches of each flow unit is calculated according to the assumptions of parabolic laminar flow and incompressibility. The detailed derivation is presented in Appendix A.

The tissue region, i.e., the gray area in Fig. 2(b), is generated by deforming and rotating a short cylinder with a radius of 17.5 mm and a height equals to the maximal diameter of the flow units. The rotation angle is a random value in the range of $[-10^\circ, 10^\circ]$, whereas the deformation matrix is defined as

$$\begin{bmatrix} 1 & 0 & 0 \\ 0 & 1 & 0 \\ 0 & 0 & 0.8 \end{bmatrix} \quad (17)$$

Respiration-mimicking tissue motions are applied to the numerical phantom (Fig. 2(c)). Specifically, finite element analysis (FEA) in FEBio [42] estimates the axial and lateral displacements under axial compression with a maximum axial strain of 2%. The compression-recovery tissue motion cycle rate is 1/3 Hz, mimicking the normal human respiration rate of 20 beats per minute.

Scatterers were randomly distributed in the tissue and flow regions at a density of 10 per resolution cell, or equally 189 mm^{-3} . The average scattering amplitude of tissue scatterers is around 20 times higher than that of flow scatterers, mimicking the contrast-free imaging scenarios. Note that the motions of flow scatterers are the combination of flow dynamics and tissue compression.

A plane wave compounding sequence is simulated in Field II [43] to image the numerical phantom. Specifically, a L10-5 linear array with a center frequency of 7.5 MHz is used to transmit 5 plane waves with steering angles of $[-10^\circ, -5^\circ, 0^\circ, 5^\circ, 10^\circ]$. The pulse repetition frequency (PRF) is 5 kHz, resulting in a frame rate of 1 kHz. The acquisition time is 6 seconds, containing a total number of 6,000 frames. Gaussian white noises with an SNR of 25 dB are added to the beamformed data. The first 5,400 frames were used to train U^2 -rPCA and 3D-Res-UNet, whereas the rest 600 frames were used for testing.

B. In-Vivo Experiments

We used the public PALA datasets provided in [44] to validate the effectiveness of U^2 -rPCA. PALA provides four *in-vivo* contrast-enhanced datasets including rat brain, rat brain bolus, rat kidney, and mouse tumor. We chose the kidney and the tumor datasets for the experiments because the selected objects are more likely to suffer from complex non-rigid motions caused by respiration and heartbeat. Both datasets were acquired with a five-angle plane wave imaging sequence running on a 15-MHz high-frequency probe. Contrast agents

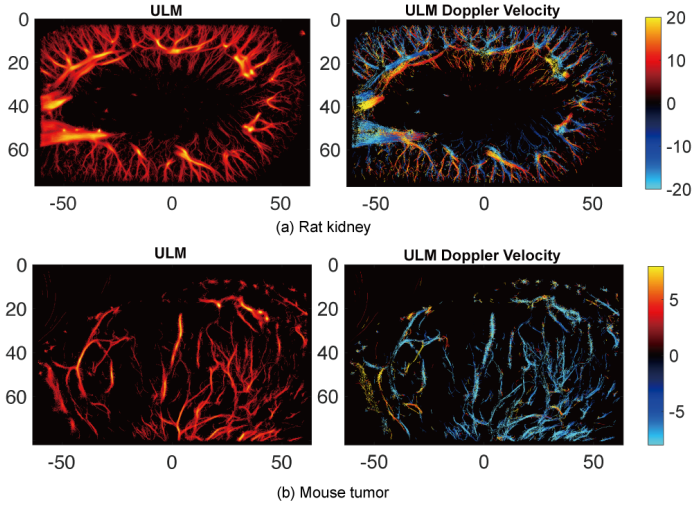


Fig. 3. ULM density maps and axial velocity components (references of the Doppler velocity estimations) of (a) the kidney dataset and (b) the tumor dataset obtained from the PALA scripts and data.

were used to enhance the visibility of blood flow. The image size is 78×128 for the kidney and 83×128 for the tumor.

Fig. 3 presents the ULM density maps and the velocity maps of the axial components of the kidney and tumor datasets. The two maps provide references to power Doppler imaging and Doppler velocity estimation. The total number of frames is 171,360 at a frame rate of 1 kHz for the kidney and 30,000 at a frame rate of 500 Hz for the tumor. In the kidney and tumor datasets, the first 14,400 frames were used to train the corresponding U^2 -rPCA networks, the next 5,000 frames were used for validation, and the rest frames were all used for testing.

C. Comparison and Evaluation Metrics

We adopted two traditional SVD and rPCA methods and one deep learning-based method (3D-Res-UNet) for comparison. The SVD-based method was realized by using the spatial similarity matrix for adaptive cutoff estimation [20]. The rPCA-based method was illustrated in Algorithm 1. Choosing IRLS-rPCA for comparison also helps to compare the performance of U^2 -rPCA to its baseline. For the rPCA method, the inner dimension d was fine-tuned from the singular rank when the singular value curve decreased to a threshold of 1% of the maximal value. The final choices were 25 and 15 for the kidney and tumor datasets, respectively. We specified λ_c as 0.01 and λ_b as 0.0004 for the kidney dataset, and 0.001 and 0.0002 for the tumor dataset. For each dataset, λ_c and λ_b were optimized through 2D searches. Similarly to [45], the search ranges are $\lambda_c \in [10^{-3}, 1]$ and $\lambda_b \in [10^{-4}, 1]$ for the kidney dataset, and $\lambda_c \in [10^{-4}, 1]$ and $\lambda_b \in [10^{-4}, 1]$ for the tumor dataset. The optimized combination of λ_c and λ_b was determined by taking visual inspections and quantitative metric measurements as references.

The 3D-Res-UNet method was proposed in [30]. This network consists of 3D convolution blocks, residual blocks, and skip connections. It learns the mapping from input compounded frames to power Doppler and outputs power Doppler

TABLE III
CNR OF POWER DOPPLER AND R^2 OF DOPPLER VELOCITY IN THE *in-silico* KIDNEY-MIMICKING PHANTOM

Models	No. frame	CNR [dB]			R^2		
		1	2	3	1	2	3
U^2 -rPCA		27.95	27.79	26.68	0.9530	0.9002	0.8458
IRLS-rPCA		16.07	23.36	19.48	0.9476	0.8975	0.8538
SVD		18.78	16.98	16.45	0.9471	0.8722	0.8536
3D-Res-UNet		8.06	10.56	9.90	-	-	-

images directly. According to [30], 3D-Res-UNet was trained with power Doppler images obtained from the SVD-based filtering as ground truths. Therefore, we strictly followed the structure of 3D-Res-UNet and trained it with the results obtained from the abovementioned SVD-based method. The training, validation, and testing datasets are the same as those applied to the realization of U^2 -rPCA.

We used contrast-to-noise ratio (CNR), signal-to-noise ratio (SNR), and peak-to-side-level (PSL) to quantitatively assess the power Doppler images. The formulations are defined as follows:

$$\text{CNR} = 10 \log_{10} \left(\frac{\text{mean}(\mathbf{PW}_{\text{blood}}) - \text{mean}(\mathbf{PW}_{\text{tissue}})}{\text{std}(\mathbf{PW}_{\text{tissue}})} \right) \quad (18)$$

$$\text{SNR} = 10 \log_{10} \left(\frac{\text{mean}(\mathbf{PW}_{\text{blood}})}{\text{std}(\mathbf{PW}_{\text{tissue}})} \right) \quad (19)$$

$$\text{PSL} = 10 \log_{10} \left(\frac{\max(\mathbf{PW}_{\text{blood}})}{\text{mean}(\mathbf{PW}_{\text{tissue}})} \right) \quad (20)$$

where $\text{mean}(\cdot)$, $\text{std}(\cdot)$, and $\max(\cdot)$ calculate the average, the standard deviation, and the maximum of the power Doppler signals, respectively. The PSL is only used to validate the effectiveness of the plug-in SEU module.

D. Implementation Details

Two hyperparameters, K and d were predefined for U^2 -rPCA. According to the parameter study presented in Sec. V-C, K was set as 5 for the kidney dataset and 4 for the tumor dataset. d was fixed to 40 and 38 for the kidney and tumor datasets, respectively. For the kidney dataset, λ_b in each layer was initialized to 20. For the tumor dataset, this penalty coefficient was initialized to 10. In simulations data, K , d , and λ_b was set as 10, 10, and 6, respectively. The size of each training batch was $N_s \times N_{\text{batch}}$. N_{batch} was set to 800 frames in the *in-vivo* dataset and 200 frames in the *in-silico* dataset. For the realization of 3D-Res-UNet, all the parameters were set according to its default and recommended configurations. Since the raw ultrasound sequences are in the in-phase and quadrature-phased (IQ) format, we expanded the traditional real-value network into a complex network. Experiments were conducted in a Linux environment using an Intel(R) Xeon(R) Silver 4210 CPU @ 2.20 GHz and an NVIDIA GeForce RTX 3090 GPU. The network was trained using the Adam optimization algorithm with an initial learning rate of 0.01 and 0.0001. An early stopping with a patience of 5 epochs was employed to avoid overfitting.

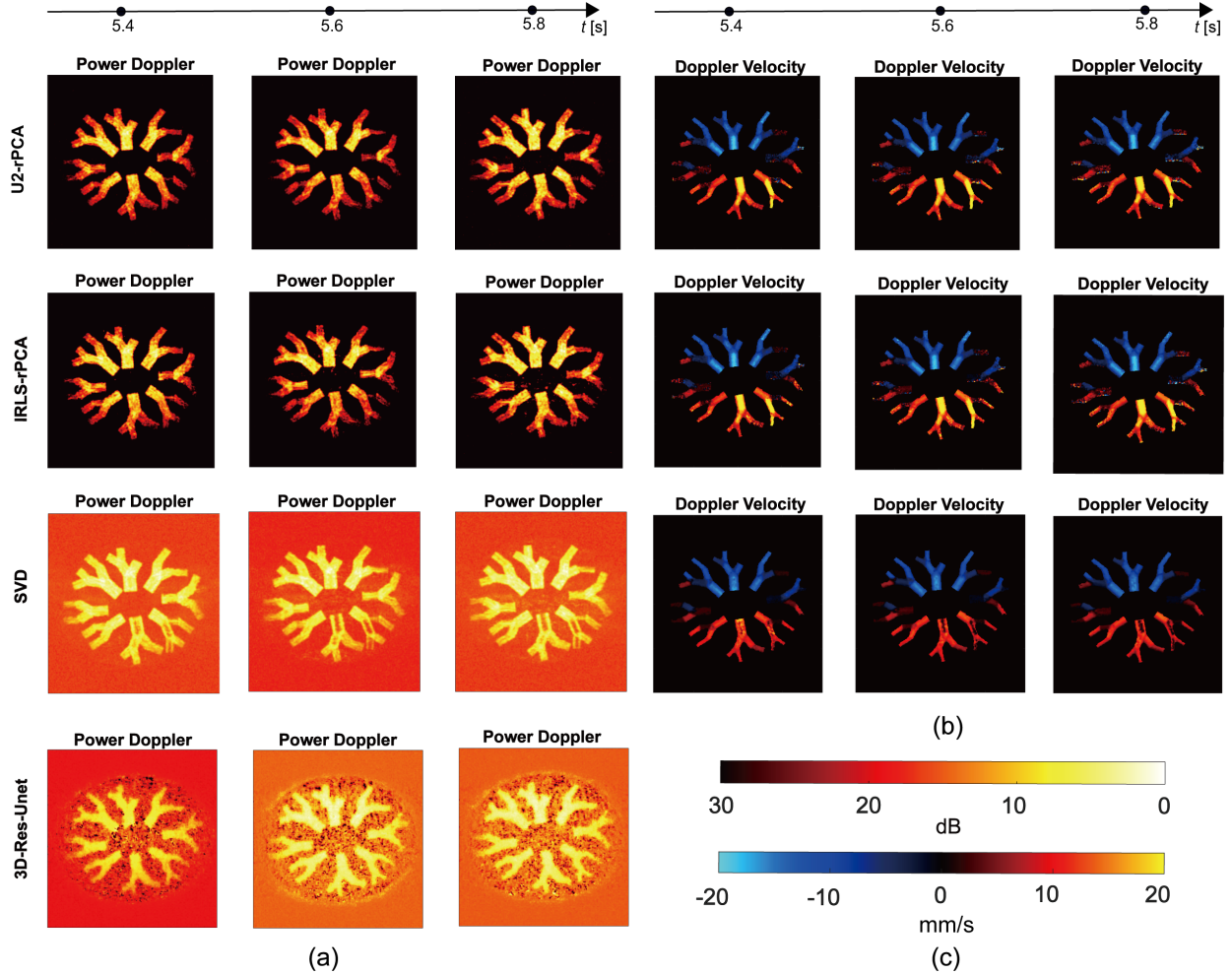


Fig. 4. (a) Power Doppler images of the *in-silico* kidney-mimicking phantom obtained by U^2 -rPCA, IRLS-rPCA, SVD, and 3D-Res-UNet. (b) Doppler velocity images obtained by U^2 -rPCA, IRLS-rPCA, and SVD. (c) The color bars illustrate the dynamic range and velocity range.

V. RESULTS

A. Simulations

Fig. 4 shows the power Doppler images and Doppler velocities of the *in-silico* kidney-mimicking phantom obtained from the last 600 frames of this dataset with an ensemble length of 200. Note that Doppler velocity is unavailable for 3D-Res-UNet because this network only outputs power Doppler estimates. In this dataset, U^2 -rPCA and IRLS-rPCA suppress tissue signals and noises to a lower level than SVD and 3D-Res-UNet in power Doppler images. In a visual comparison, U^2 -rPCA and IRLS-rPCA achieve similar estimates of power Doppler and Doppler velocities. In addition, SVD loses some flow signals in the 6th and 7th flow units, leaving hollows in power Doppler images and the corresponding Doppler velocities.

Table III lists the CNRs of the power Doppler images and the correlations (R^2) between the estimated Doppler estimates and the ground truths. The tissue and flow ROIs for CNR calculation are delineated from the ground truth regions in Fig. 2. U^2 -rPCA achieves the highest CNRs in all three power Doppler images, whereas IRLS-rPCA ranks the second best in the 2nd and 3rd images. In terms of Doppler velocity, the tested

methods achieve comparable correlations when compared with the ground truths. Although SVD cannot correctly estimate Doppler velocities in the hollow regions in the 6th and 7th flow units, it provides smoother estimates in the 1st and 5th flow units than U^2 -rPCA and IRLS-rPCA, where the flow directions are generally parallel to the probe.

B. In-Vivo Experiments

Fig. 5 shows the power Doppler images of the rat kidney obtained by U^2 -rPCA, IRLS-rPCA, SVD, and 3D-Res-UNet. Two region-of-interests (ROIs) are zoomed in for a clearer interpretation. It can be observed that U^2 -rPCA and IRLS-rPCA achieve better clutter suppression than SVD and 3D-Res-UNet, showing more highlighted vessels and lower tissue signals. Since the 3D-Res-UNet method was trained using the results of SVD, its performance is similar to its SVD counterparts. A closer observation on the zoomed-in regions of Fig. 5(a) and Fig. 5(b) demonstrates that U^2 -rPCA better distinguishes the microvessels from surrounding tissues, showing more distinct differences between power signals of microvessels and tissues.

Fig. 6 shows the power Doppler images of the mouse tumor with two zoomed-in ROIs. The results of this dataset are sim-

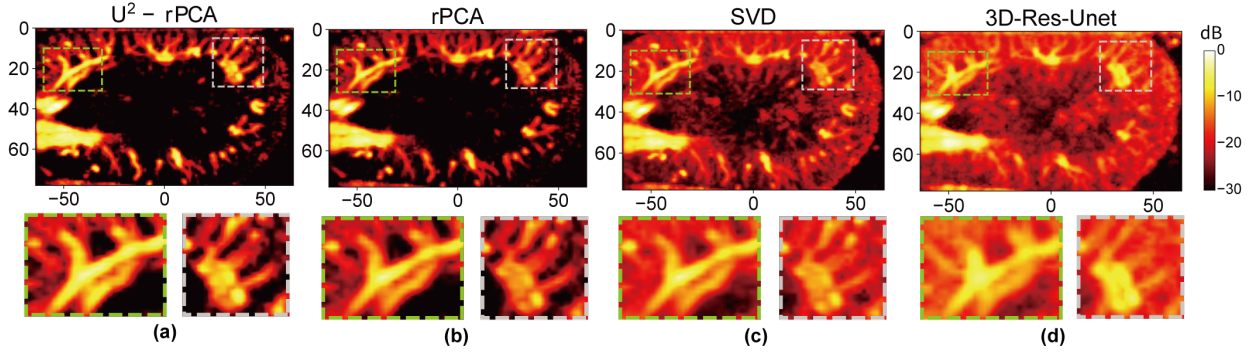


Fig. 5. Power Doppler images of the kidney obtained by (a) U^2 -rPCA, (b) IRLS-rPCA, (c) SVD, and (d) 3D-Res-UNet.

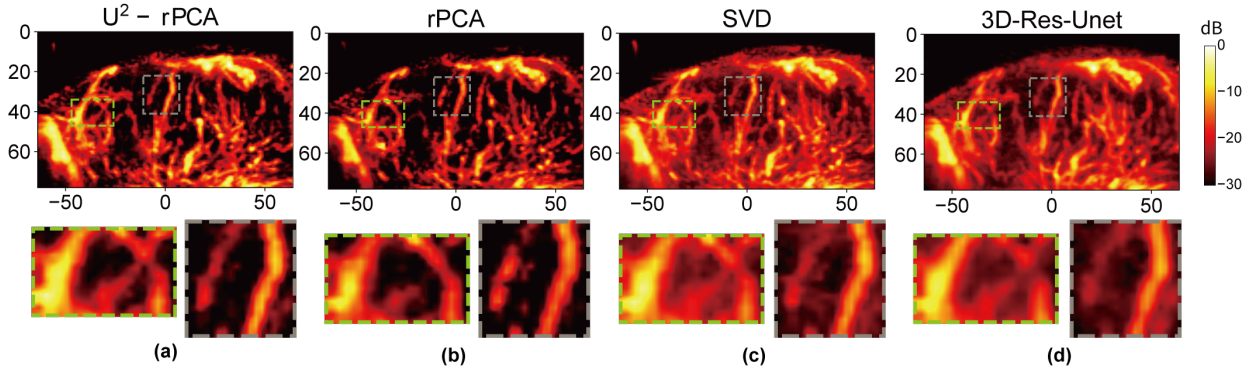


Fig. 6. Power Doppler images of the tumor obtained by (a) U^2 -rPCA, (b) IRLS-rPCA, (c) SVD, and (d) 3D-Res-UNet.

TABLE IV
CNR AND SNR ON TWO ROIS OF THE TWO *In-vivo* DATASETS (UNIT: DB).

	ROI 1 for rat kidney		ROI 2 for rat kidney		ROI 1 for mouse tumor		ROI 2 for mouse tumor	
	CNR	SNR	CNR	SNR	CNR	SNR	CNR	SNR
SVD	18.62±1.74	18.75±1.70	17.94±1.73	17.27±1.09	29.09±3.67	29.12±3.65	27.92±4.04	27.97±4.00
IRLS-rPCA	25.25±2.21	25.26±2.20	24.20±2.22	24.23±2.21	32.34±9.39	32.40±9.25	30.53±9.73	30.59±9.60
3D-Res-UNet	18.57±1.36	18.71±1.33	17.21±1.61	17.42±1.57	30.90±1.26	30.94±1.25	30.22±2.12	30.27±2.10
U^2 -rPCA	27.91±2.19	27.91±2.18	26.42±1.99	26.43±1.99	34.25±7.26	34.27±7.23	33.09±7.67	33.11±7.63

ilar to those of the kidney dataset. The rPCA-based methods (U^2 -rPCA and IRLS-rPCA) generally achieve better clutter filtering effects than the SVD-based methods (SVD and 3D-Res-UNet). Furthermore, U^2 -rPCA separates the microvessels more clearly than IRLS-rPCA.

Table. IV lists the CNR and SNR of the power Doppler images. Since CNR and SNR are region-dependent local metrics, we delineated two blood flow and tissue ROIs for each dataset. The delineation of ROI obeys the following principles. First, the tissue ROIs lie in the regions without visible blood flow signals. Second, the blood flow ROIs are restricted in the interior of vessels which are resolved by all the tested methods. Finally, the tissue ROI and blood flow ROI have similar areas. Table. IV clearly illustrates that U^2 -rPCA achieves the highest CNR and SNR on both datasets among the tested methods.

Particularly, in the kidney dataset, U^2 -rPCA improves CNR by over 8.48 dB when compared with SVD and 3D-Res-UNet, and over 2.22 dB when compared with IRLS-rPCA. In the tumor dataset, the improvements of CNR achieved by U^2 -rPCA are over 2.87 dB versus SVD and 3D-Res-UNet, and over 1.91 dB versus IRLS-rPCA.

Fig. 7 plots the signal intensities after logarithmic compression of the cross-section indicated by the white dashed lines. The profiles of the ULM density maps provided by PALA are also presented as references. For both datasets, one can see that U^2 -rPCA and IRLS-rPCA suppress more tissue signals than SVD and 3D-Res-UNet, showing a lower level of side lobes. When inspecting the main lobes that indicate the resolved microvessels, it can be roughly justified that all the tested methods depict the vessels under comparable main lobe

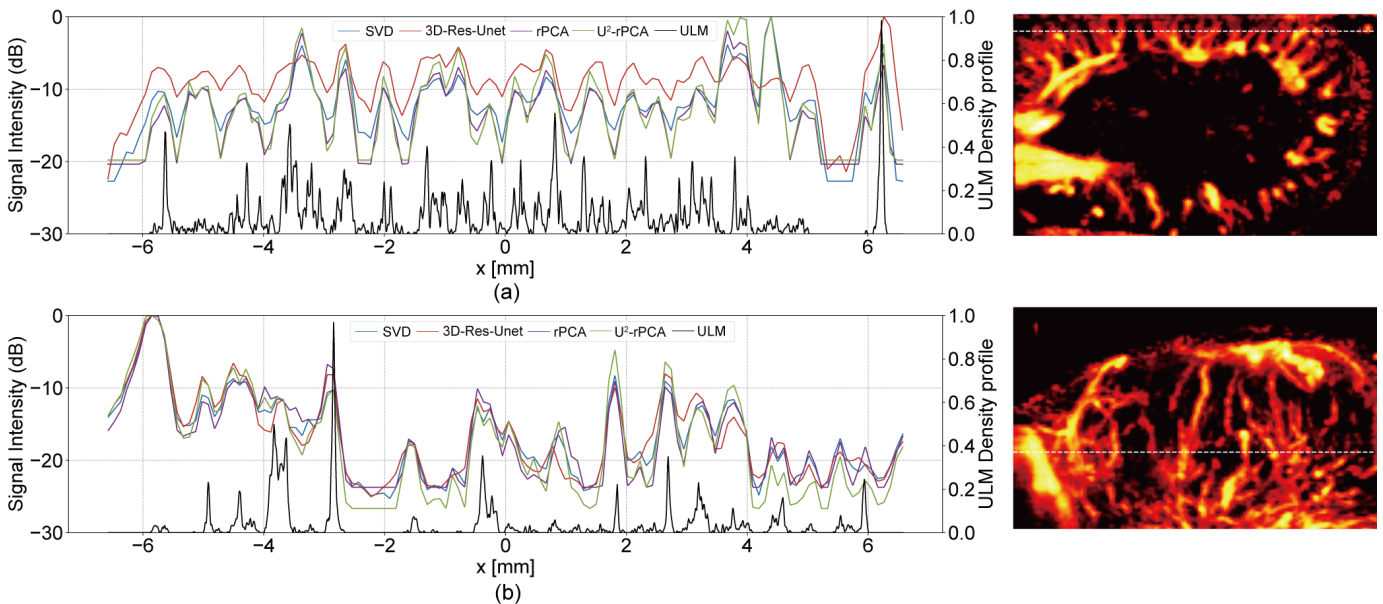


Fig. 7. The normalized signal intensities (in dB) of the selected cross-section for (a) the kidney dataset and (b) the tumor dataset.

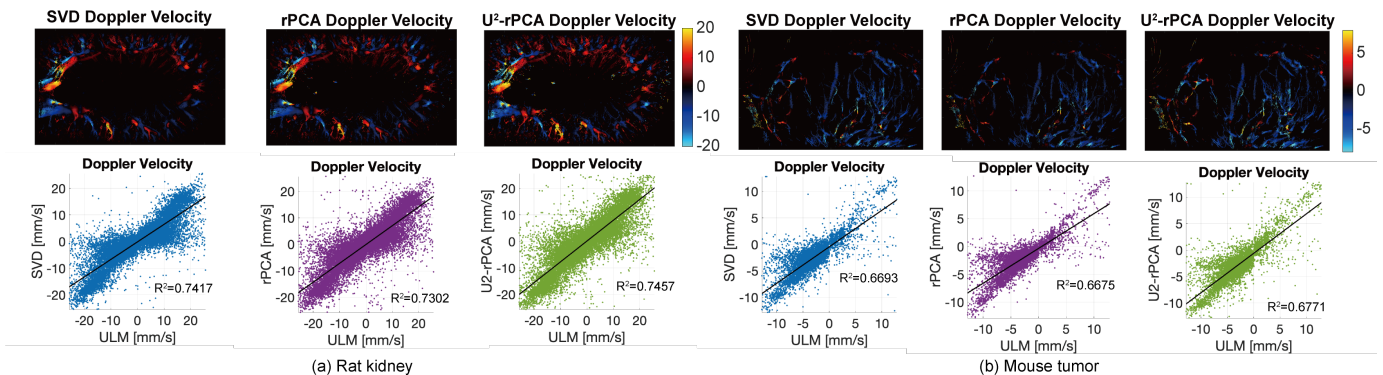


Fig. 8. Doppler velocity images and the corresponding correlations between the estimates and ground truths provided by PALA in (a) the kidney dataset and (b) the tumor dataset.

TABLE V
FRAME RATE (FPS) OF THE TESTED METHODS IN THE RAT KIDNEY DATASET AND THE MOUSE TUMOR DATASET.

		SVD	IRLS-rPCA	3D-Res-UNet	U ² -rPCA w/o SEU	U ² -rPCA w/ SEU
Rat kidney	CPU	83.70±19.17	29.95±0.47	1020.16±48.50	340.56±7.82	31.45±0.64
	GPU	/	/	2146.36±238.68	1307.30±417.25	136.61±14.37
Mouse tumor	CPU	91.88±14.94	137.85±7.20	1021.81±49.14	942.74±97.12	78.96±3.56
	GPU	/	/	2201.53±174.55	2273.67±496.27	163.84±5.50

widths, showing similar capabilities in terms of spatial resolution. The profiles demonstrate that SVD-based and rPCA-based clutter filtering methods have similar performances in the spatial resolution of power Doppler images.

Fig. 8 presents the Doppler velocities estimated by SVD, IRLS-rPCA, and U²-rPCA in the two datasets. Visual inspection and the reported correlations demonstrate that the tested methods have comparable performance in terms of Doppler velocity estimation. This is rational because there is no evidence to show that SVD or rPCA can provide more accurate Doppler velocity estimations than the other. In

addition, the fitted lines reveal underestimations of the Doppler velocities compared to the ground truths. This is because the microvessel size is relatively small compared with the full-width-half-maximum (FWHM) of the ultrasound beam in the elevation dimension [46]. The ground-truth axial velocities in PALA do not encounter this issue because the velocities were estimated via microbubble localization and tracking rather than Doppler estimation.

Table V lists the average computational time in the unit of frames per second (fps) achieved by the tested methods. The inference time of 3D-Res-UNet and U²-rPCA was measured

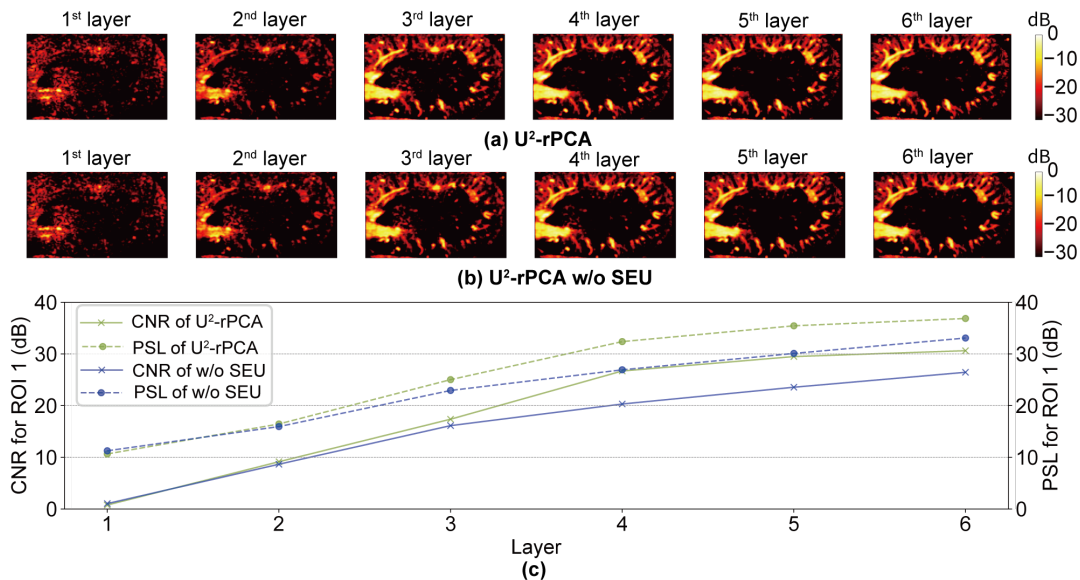


Fig. 9. Influences of the number of layers K on U²-rPCA in the kidney dataset. The layer-by-layer power Doppler images outputs of (a) U²-rPCA and (b) U²-rPCA w/o SEU. (c) Corresponding CNR and PSL curves.

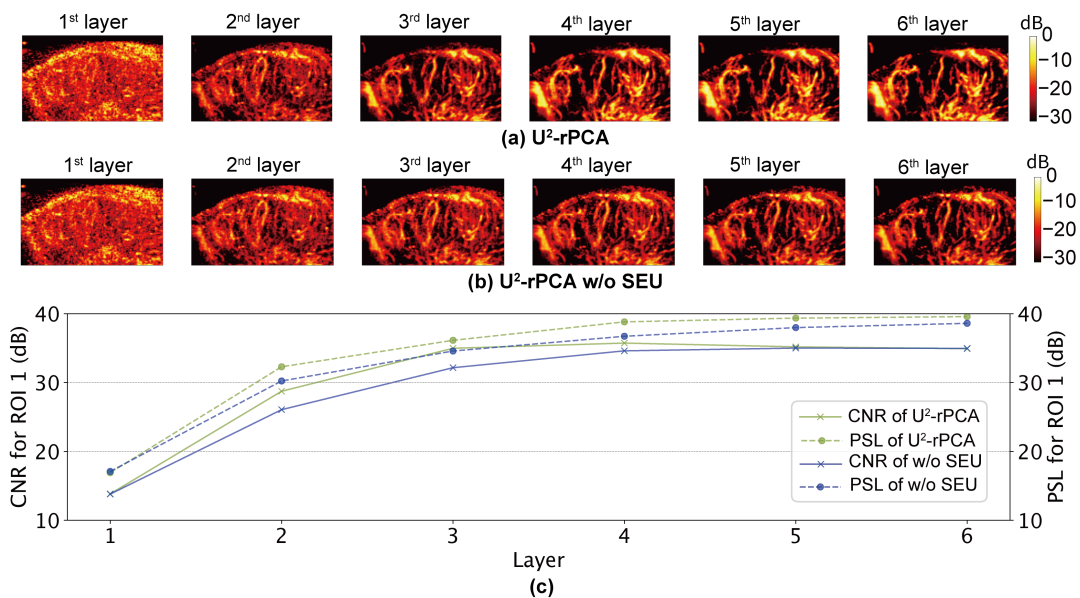


Fig. 10. Influences of the number of layers K on U²-rPCA in the tumor dataset. The layer-by-layer power Doppler images outputs of (a) U²-rPCA and (b) U²-rPCA w/o SEU. (c) Corresponding CNR and PSL curves.

on CPU and GPU platforms. In summary, all the tested methods meet the basic requirement of real-time implementation, which is around 30 fps. Notably, the SEU module has a negative impact on the inference efficiency of U²-rPCA, showing a deceleration factor of around 10 when this module is plugged into the U²-rPCA networks.

C. Parameter Study

This subsection investigates the influences of two key hyperparameters on U²-rPCA. The first hyperparameter is the number of layers, K , of the U²-rPCA network. Fig. 9 and 10 present the layer-by-layer power Doppler images output by U²-rPCA in the kidney and tumor dataset, respectively.

The outputs of U²-rPCA without the SEU module are also presented for comparison. It can be seen that the power Doppler images are improved when K increases from 1 to 6, which are demonstrated by the CNR curves. Particularly, in Fig. 10, the outputs of U²-rPCA become stable, showing that the CNR curve enters the plateau phase when K is larger than 3. In Fig. 9, although the CNR curve slightly increases when K is larger than 3, the power Doppler images show little variance via visual inspection. Therefore, we finally adopted $K = 5$ and $K = 4$ for the kidney and tumor datasets, respectively.

Fig. 9 and 10 also demonstrate the effectiveness of SEU. Specifically, Fig. 9 shows an improvement of around 5 dB in SPL with SEU when K is larger than 3. In the tumor dataset,

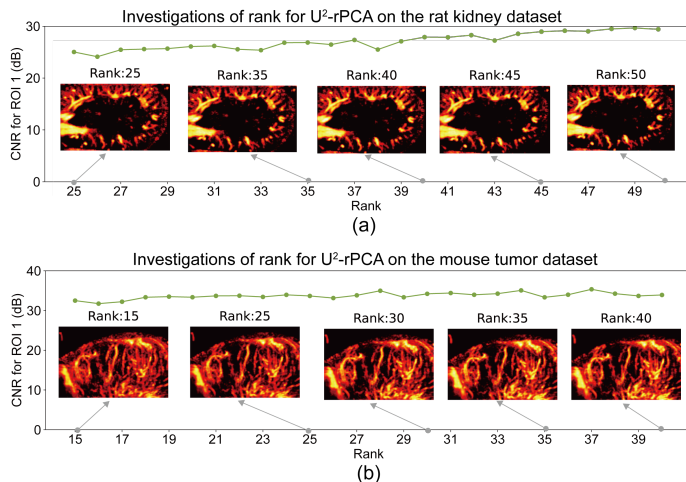


Fig. 11. The influences of the inner dimension d on U^2 -rPCA in (a) the kidney dataset and (b) the tumor dataset.

the average improvement achieved with SEU is around 2 dB when K is larger than 3.

Fig. 11 investigates the influences of the inner dimension, d , on U^2 -rPCA. The IRLS-rPCA baseline uses $d = 25$ and $d = 15$ for the kidney and tumor datasets, respectively. Consider that a large d allows the matrix \mathbf{U} to store more features about the tissue signals, we investigated the performance of U^2 -rPCA by increasing d from 25 to 50 in kidney and 15 to 40 in tumor. However, Fig. 11 shows limited influences of this hyperparameter on U^2 -rPCA, demonstrating the robustness of this method to the inner dimension. As a result, we empirically chose $d = 40$ and $d = 38$ for the kidney and tumor datasets, respectively.

VI. DISCUSSION

This paper proposes U^2 -rPCA that performs clutter filtering via deep learning. The network is unfolded from an IRLS-rPCA baseline in which both the low-rank and sparse terms are modeled with differential Frobenius norms. The MSE loss is equivalently applied to train the network in an unsupervised manner without losing interpretability. Experimental validations on the *in-silico* and public *in-vivo* datasets demonstrated the outperformance of U^2 -rPCA by comparing it with other methods. In the following section, we present more insights into the effectiveness of U^2 -rPCA and discuss the limitations and perspective of this paper.

A. Effectiveness Analysis

Unsupervised training is one of the most representative characteristics of U^2 -rPCA. Nevertheless, unsupervised training is a double-edged sword. On the one hand, the filter is insusceptible to the training data, particularly when the *in-vitro* and *in-vivo* ground truths are inaccessible. On the other hand, the network behaves similarly to its rPCA baseline because it has no opportunity to learn from high-quality references. To this end, we added SEU to each layer to strengthen the network's capability in resolving the sparse microflow signals. The layer-by-layer interpretations in Figs. 9 and 10

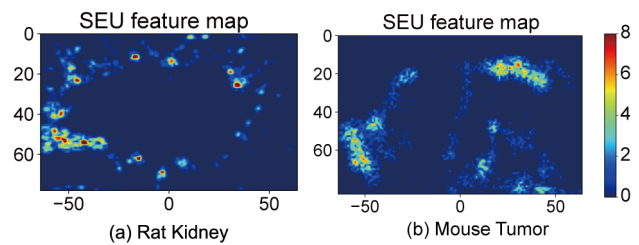


Fig. 12. Visualization of feature maps extracted from SEU in (a) the kidney dataset and (b) the tumor dataset.

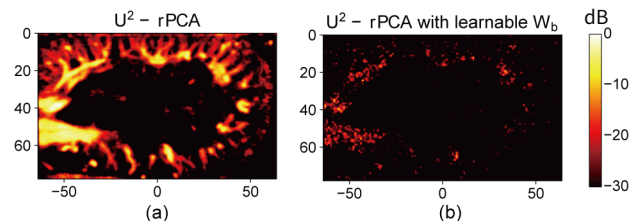


Fig. 13. Power Doppler images obtained by (a) U^2 -rPCA and (b) U^2 -rPCA with learnable \mathbf{W}_b in the kidney dataset.

demonstrate the effectiveness of SEU, showing improvements in the quality of power Doppler images. Furthermore, Fig. 12 visualizes the feature maps output by SEU in the two datasets. It can be seen that SEU focuses more on the flow, i.e., sparse regions. These characteristics are the main reason why SEU can improve the effectiveness of power Doppler imaging.

However, the cost of adding SEU is much longer inference time, as illustrated in Table V. Although the frame rate of U^2 -rPCA with SEU still exceeds 30 fps, the network without SEU achieves frame rates over 1 KHz. This is because the SEU module contains extensive learnable parameters. For example, the U^2 -rPCA network has 3.1M and 3.08M learnable parameters per layer with SEU for the kidney and tumor datasets, respectively. However, this number significantly decreases to 1.6k and 1.45k per layer when SEU is removed. As a result, we recommend setting SEU as a plug-in module. Whether to use this module or not depends on the task's priority, e.g., image quality or computational efficiency.

One may wonder why U^2 -rPCA sets \mathbf{W}_b as deterministic and \mathbf{W}_c as learnable. This is because \mathbf{W}_b is strongly connected to the blood flow signals \mathbf{B} , as denoted in Eq. (7). The IRLS relationship of \mathbf{B} and \mathbf{W}_b is mathematically equivalent to the l_1 -norm sparse modeling. Setting \mathbf{W}_b as deterministic parameters applies intrinsic sparse regularization to U^2 -rPCA. On the other hand, the low rankness of U^2 -rPCA is regularized by the tissue basis \mathbf{U} since $\mathbf{T} = \mathbf{U}\mathbf{V}^*$ and \mathbf{U} is itself low-rank. The intrinsic low-rank and sparse regularization make the network mathematically interpretable. As a result, U^2 -rPCA can be trained by solely adopting the data consistency term as the loss function (see Eq. (16)). To experimentally validate the above analyses, we set \mathbf{W}_b as learnable parameters to break the connection between \mathbf{B} and \mathbf{W}_b . The resulting power Doppler image of the kidney is presented in Fig. 13, showing that the learnable \mathbf{W}_b results in the failure of U^2 -rPCA. The network can no longer extract effective blood flow signals from the input frames.

B. Limitation and Perspective

The *in-silico* experiments were conducted to mimic the contrast-free imaging scenarios. Because the original objective and ultimate goal of this work are a U²-rPCA clutter filter for contrast-free microvascular imaging. The consideration is that contrast-free ultrasound microvascular imaging may be more universal in real clinical routines because not all patients are suitable to undergo contrast agent (microbubble) injection. Unfortunately, it is difficult to find or collect such types of public or private ultrasound datasets for the deep learning-based clutter filtering methods in the current circumstances. As an alternative, we referred to the contrast-enhanced PALA datasets because they contain several different imaging targets with long enough acquisitions for network training. In addition, the ULM results also provide references to evaluate the effectiveness of the tested methods. Applying U²-rPCA to the real contrast-free imaging scenarios is one of the most important directions of our future work.

Although U²-rPCA relieves us from extensively collecting and annotating training data, the network cannot learn abundant features of referenced tissue and blood flow signals. However, the current supervised clutter filters are limited by high-quality ground truths. The strategies of convolving moving scatterers with PSF cannot fully mimic complex microvascular imaging conditions, whereas the *in-vitro* and *in-vivo* ground-truths are technically inaccessible. Nevertheless, the potential of supervised deep filtering should be treated seriously. Recently, several realistic contrast-enhanced ultrasound simulators have been proposed to mimic the morphology and hemodynamics of microvascular networks and their interactions with ultrasound [47]–[50]. These simulators could help the deep learning-based methods reach a better balance in suppressing clutter and preserving blood flow signals.

VII. CONCLUSION

This paper proposes an unsupervised unfolded rPCA clutter filtering method named U²-rPCA for ultrasound microvascular imaging. The network was unfolded from an IRLS-rPCA baseline and trained in an unsupervised manner with mathematical interpretability. Experimental validations on the *in-silico* and public *in-vivo* datasets demonstrated the outperformance of U²-rPCA when compared with the SVD method, the rPCA baseline, and another deep learning-based clutter filter. The effectiveness of the modules that construct U²-rPCA was validated through ablation studies. Improving the training scheme and introducing semi-supervised learning to strengthen the performance of the proposed method are the future work of this paper.

APPENDIX A

According to [51] and taking the complete flow unit for example, the incidence matrix is

$$\mathbf{A} = \begin{bmatrix} -1 & 1 & 0 & 0 & 0 & 0 & 0 & 0 \\ 0 & -1 & 1 & 0 & 0 & 0 & 0 & 0 \\ 0 & -1 & 0 & 1 & 0 & 0 & 0 & 0 \\ 0 & 0 & -1 & 0 & 1 & 0 & 0 & 0 \\ 0 & 0 & -1 & 0 & 0 & 1 & 0 & 0 \\ 0 & 0 & 0 & -1 & 0 & 0 & 1 & 0 \\ 0 & 0 & 0 & -1 & 0 & 0 & 0 & 1 \end{bmatrix} \quad (21)$$

where the 7 edges and 8 nodes lie in the row and column dimensions, respectively.

By separating \mathbf{A} into two sub-matrices \mathbf{A}_h and \mathbf{A}_{nh} that containing the hanging (orange dots in Fig. 2(a)) and non-hanging nodes (green dots in Fig. 2(a)), the pressure differences across edges are formulated as

$$d\mathbf{P}_e = \mathbf{A}_h \mathbf{P}_h + \mathbf{A}_{nh} \mathbf{P}_{nh} \quad (22)$$

where \mathbf{P}_h and \mathbf{P}_{nh} are the pressures of the hanging and non-hanging nodes, respectively. The incompressibility assumption restricts the sum of flows in each non-hanging node to zero:

$$\mathbf{A}_{nh}^\top \mathbf{Q}_e = 0 \quad (23)$$

where \mathbf{Q}_e is a vector that contains the flows of edges. \mathbf{Q}_e and $d\mathbf{P}_e$ are linearly connected through an edge conductance matrix according to the Hagen–Poiseuille law:

$$\mathbf{Q}_e = \mathbf{C} \cdot d\mathbf{P}_e \quad (24)$$

\mathbf{C} is a diagonal matrix containing the flow conductance of each edge:

$$\mathbf{C} = \text{diag} \left(\left[\frac{1}{\xi_1}, \dots, \frac{1}{\xi_7} \right] \right) \quad (25)$$

ξ is defined as:

$$\xi = \frac{8\mu L}{\pi R^4} \quad (26)$$

where $\mu \approx 0.004 \text{ Pa} \cdot \text{s}$ is the kinematic viscosity of blood.

Since \mathbf{P}_h is known or determined manually, \mathbf{P}_{nh} is expressed as

$$\mathbf{P}_{nh} = -(\mathbf{A}_{nh}^\top \mathbf{C} \mathbf{A}_{nh})^{-1} \mathbf{A}_{nh}^\top \mathbf{C} \mathbf{A}_h \mathbf{P}_h \quad (27)$$

In addition, the relationship between the maximum velocity v_{max} and pressure difference dP_e of an edge is

$$v_{max} = \frac{R^2}{4\mu} dP_e \quad (28)$$

Finally, by adjusting \mathbf{P}_h , the maximal velocity of the first hierarchy can be adjusted to a random value between 20 mm/s and 30 mm/s. The maximal velocities of the other hierarchies are determined accordingly.

REFERENCES

- [1] O. Couture, V. Hingot, B. Heiles, P. Muleki-Seya, and M. Tanter, "Ultrasound localization microscopy and super-resolution: A state of the art," *IEEE Trans. Ultrason. Ferroelectr. Freq. Control*, vol. 65, no. 8, pp. 1304–1320, 2018.
- [2] H. Yi, M. R. Lowerison, P. Song, and W. Zhang, "A review of clinical applications for super-resolution ultrasound localization microscopy," *Curr. Med. Sci.*, vol. 42, pp. 1–16, 2022.
- [3] Z. Kou, M. R. Lowerison, Q. You, Y. Wang, P. Song, and M. L. Oelze, "High-resolution power doppler using null subtraction imaging," *IEEE Trans. Med. Imag.*, vol. 43, pp. 3060–3071, 2023.
- [4] C. Deme n e, T. Deffieux, M. Pernot, B.-F. Osmanski, V. Biran, J.-L. Gennisson *et al.*, "Spatiotemporal clutter filtering of ultrafast ultrasound data highly increases Doppler and ultrasound sensitivity," *IEEE Trans. Med. Imag.*, vol. 34, no. 11, pp. 2271–2285, Nov. 2015.
- [5] L. Huang, J. Zhang, X. Wei, L. Jing, Q. He, X. Xie, G. Wang, and J. Luo, "Improved ultrafast power doppler imaging by using spatiotemporal non-local means filtering," *IEEE Trans. Ultrason. Ferroelectr. Freq. Control*, vol. 69, no. 5, pp. 1610–1624, 2022.
- [6] M. Bayat and M. Fatemi, "Concurrent clutter and noise suppression via low rank plus sparse optimization for non-contrast ultrasound flow Doppler processing in microvasculature," in *2018 IEEE International Conference on Acoustics, Speech and Signal Processing (ICASSP)*. IEEE, 2018, pp. 1080–1084.
- [7] H. Wang, S. Gao, M. Mozumi, M. Omura, R. Nagaoka, and H. Hasegawa, "Preliminary investigation on clutter filtering based on deep learning," *Jpn. J. Appl. Phys.*, vol. 60, no. SD, p. SDDE21, 2021.
- [8] S. Ehrenstein, E. Abenojar, R. Perera, A. Exner, and M. Bayat, "Rank-assisted deep residual reconstruction network for non-contrast ultrasound imaging of blood microvessels," in *2021 IEEE International Ultrasonics Symposium (IUS)*. IEEE, 2021, pp. 1–4.
- [9] M. Tabassian, X. Hu, B. Chakraborty, and J. D'hooge, "Clutter filtering using a 3d deep convolutional neural network," in *2019 IEEE International Ultrasonics Symposium (IUS)*. IEEE, 2019, pp. 2114–2117.
- [10] K. Gregor and Y. LeCun, "Learning fast approximations of sparse coding," in *Proc. 27th Int. Conf. Mach. Learn.*, 2010, pp. 399–406.
- [11] V. Monga, Y. Li, and Y. C. Eldar, "Algorithm unrolling: Interpretable, efficient deep learning for signal and image processing," *IEEE Signal Process. Mag.*, vol. 38, no. 2, pp. 18–44, 2021.
- [12] N. Shlezinger, Y. C. Eldar, and S. P. Boyd, "Model-based deep learning: on the intersection of deep learning and optimization," *IEEE Access*, vol. 10, pp. 115 384–115 398, 2022.
- [13] P. Zhang, S. Ren, Y. Liu, Z. Gui, H. Shangguan, Y. Wang, H. Shu, and Y. Chen, "A total variation prior unrolling approach for computed tomography reconstruction," *Med. Phys.*, vol. 50, no. 5, pp. 2816–2834, 2023.
- [14] P. Huang, C. Zhang, X. Zhang, X. Li, L. Dong, and L. Ying, "Self-supervised deep unrolled reconstruction using regularization by denoising," *IEEE Trans. Med. Imaging*, vol. 43, no. 3, pp. 1203–1213, 2024.
- [15] Y. Huang, J. Zhao, Z. Wang, V. Orekhov, D. Guo, and X. Qu, "Exponential signal reconstruction with deep hankel matrix factorization," *IEEE Trans. Neural Netw. Learn. Syst.*, vol. 34, no. 9, pp. 6214–6226, 2021.
- [16] A. Mamistvalov and Y. C. Eldar, "Deep unfolded recovery of sub-nyquist sampled ultrasound images," *IEEE Trans. Ultrason. Ferroelectr. Freq. Control*, vol. 68, no. 12, pp. 3484–3496, 2021.
- [17] C. Khan, R. J. van Sloun, and B. Byram, "Unfolding model-based beamforming for high quality ultrasound imaging," in *2022 IEEE International Conference on Acoustics, Speech and Signal Processing (ICASSP)*. IEEE, 2022, pp. 8682–8686.
- [18] B. Joukovsky, Y. C. Eldar, and N. Deligiannis, "Interpretable neural networks for video separation: deep unfolding rPCA with foreground masking," *IEEE Trans. Image Process.*, vol. 33, pp. 108–122, 2024.
- [19] P. Song, A. Manduca, J. D. Trzasko, and S. Chen, "Ultrasound small vessel imaging with block-wise adaptive local clutter filtering," *IEEE Trans. Med. Imag.*, vol. 36, no. 1, pp. 251–262, 2016.
- [20] J. Baranger, B. Arnal, F. Perren, O. Baud, M. Tanter, and C. Deme n e, "Adaptive spatiotemporal SVD clutter filtering for ultrafast Doppler imaging using similarity of spatial singular vectors," *IEEE Trans. Med. Imag.*, vol. 37, no. 7, pp. 1574–1586, Jul. 2018.
- [21] J. Baranger, J. Aguet, and O. Villemain, "Fast thresholding of SVD clutter filter using the spatial similarity matrix and a sum-table algorithm," *IEEE Trans. Ultrason. Ferroelectr. Freq. Control*, vol. 70, no. 8, pp. 821–830, Aug. 2023.
- [22] S. A. Waraich, A. Chee, D. Xiao, B. Y. Yiu, and A. Yu, "Auto SVD clutter filtering for US Doppler imaging using 3D clustering algorithm," in *Image Analysis and Recognition: 16th International Conference, ICIAR 2019*. Springer, 2019, pp. 473–483.
- [23] Y. Chen, B. Fang, F. Meng, J. Luo, and X. Luo, "Competitive swarm optimized SVD clutter filtering for ultrafast power Doppler imaging," *IEEE Trans. Ultrason. Ferroelectr. Freq. Control*, vol. 71, no. 4, pp. 459–473, 2024.
- [24] B. Fang, F. Meng, Y. Chen, J. Luo, and X. Luo, "A competitive swarm optimized SVD-based clutter filter," in *2023 IEEE International Ultrasonics Symposium (IUS)*. IEEE, 2023, pp. 1–4.
- [25] K. Xu, X. Guo, Y. Sui, V. Hingot, O. Couture, D. Ta *et al.*, "Robust pca-based clutter filtering method for super-resolution ultrasound localization microscopy," in *2021 IEEE International Ultrasonics Symposium (IUS)*, 2021, pp. 1–4.
- [26] Y. Sui, S. Yan, J. Yu, J. Song, D. Ta, W. Wang *et al.*, "Randomized spatial downsampling-based cauchy-rpca clutter filtering for high-resolution ultrafast ultrasound microvasculature imaging and functional imaging," *IEEE Trans. Ultrason. Ferroelectr. Freq. Control*, vol. 69, no. 8, pp. 2425–2436, Aug. 2022.
- [27] O. Solomon, R. Cohen, Y. Zhang, Y. Yang, Q. He, J. Luo *et al.*, "Deep unfolded robust PCA with application to clutter suppression in ultrasound," *IEEE Trans. Med. Imag.*, vol. 39, no. 4, pp. 1051–1063, Apr. 2020.
- [28] C.-H. Shih and M.-L. Li, "Power Doppler imaging with a novel convolutional autoencoder based clutter filtering technique: feasibility study," in *2019 IEEE International Ultrasonics Symposium (IUS)*, 2019, pp. 2249–2251.
- [29] K. G. Brown, D. Ghosh, and K. Hoyt, "Deep learning of spatiotemporal filtering for fast super-resolution ultrasound imaging," *IEEE Trans. Ultrason. Ferroelectr. Freq. Control*, vol. 67, no. 9, pp. 1820–1829, Sep. 2020.
- [30] T. Di Ianni and R. D. Airan, "Deep-fus: A deep learning platform for functional ultrasound imaging of the brain using sparse data," *IEEE Trans. Med. Imag.*, vol. 41, no. 7, pp. 1813–1825, Jul. 2022.
- [31] A. T. Minhaz, M. Cooley, A. Subramaniam, A. Exner, F. Orge, D. Wilson *et al.*, "End-to-end deep learning for tuning-free non-contrast ultrasound microvessel imaging," in *2022 IEEE International Ultrasonics Symposium (IUS)*. IEEE, 2022, pp. 1–3.
- [32] V. Pustovalov, D. H. Pham, and D. Kouam e, "Deep unfolding rPCA for high resolution flow estimation," in *2022 IEEE International Ultrasonics Symposium (IUS)*. IEEE, 2022, pp. 1–4.
- [33] N. Vaswani, T. Bouwmans, S. Javed, and P. Narayanamurthy, "Robust subspace learning: robust PCA, robust subspace tracking, and robust subspace recovery," *IEEE Signal Process. Mag.*, vol. 35, no. 4, pp. 32–55, 2018.
- [34] T. Bouwmans, S. Javed, H. Zhang, Z. Lin, and R. Otazo, "On the applications of robust PCA in image and video processing," *Proc. IEEE*, vol. 106, no. 8, pp. 1427–1457, 2018.
- [35] S. P. Boyd, N. Parikh, E. Chu, B. Peleato, and J. Eckstein, "Distributed optimization and statistical learning via the alternating direction method of multipliers," *Found. Trends Mach. Learn.*, vol. 3, pp. 1–122, 2011. [Online]. Available: <https://api.semanticscholar.org/CorpusID:51789432>
- [36] E. J. Cand es, X. Li, Y. Ma, and J. Wright, "Robust principal component analysis?" *J. ACM*, vol. 58, no. 3, pp. 1–37, 2011.
- [37] I. Daubechies, R. A. DeVore, M. Fornasier, and C. S. Gunt urk, "Iteratively reweighted least squares minimization for sparse recovery," *Commun. Pure Appl. Math.*, vol. 63, no. 1, pp. 1–38, 2010.
- [38] P. V. Giampouras, A. A. Rontogiannis, and K. D. Koutroumbas, "Alternating iteratively reweighted least squares minimization for low-rank matrix factorization," *IEEE Trans. Signal Process.*, vol. 67, no. 2, pp. 490–503, 2019.
- [39] A. A. Rontogiannis, P. V. Giampouras, and K. D. Koutroumbas, "Online reweighted least squares robust PCA," *IEEE Singal Process. Lett.*, vol. 27, pp. 1340–1344, 2020.
- [40] Y. Han and J. C. Ye, "Framing U-Net via deep convolutional framelets: application to sparse-view CT," *IEEE Trans. Med. Imag.*, vol. 37, no. 6, pp. 1418–1429, Jun. 2018.
- [41] K. Takeda and T. Sakai, "Unsupervised deep learning of foreground objects from low-rank and sparse dataset," *Comput. Vis. Image Underst.*, vol. 240, p. 103939, 2024.
- [42] S. A. Maas, B. J. Ellis, G. A. Ateshian, and J. A. Weiss, "Febio: Finite elements for biomechanics." *ASME. J Biomech Eng.*, vol. 134, no. 1, p. 011005, 2012.
- [43] J. Jensen and N. Svendsen, "Calculation of pressure fields from arbitrarily shaped, apodized, and excited ultrasound transducers," *IEEE*

- Transactions on Ultrasonics, Ferroelectrics, and Frequency Control*, vol. 39, no. 2, pp. 262–267, 1992.
- [44] B. Heiles, A. Chavignon, V. Hingot, P. Lopez, E. Teston, and O. Couture, “Performance benchmarking of microbubble-localization algorithms for ultrasound localization microscopy,” *Nat. Biomed. Eng.*, vol. 6, no. 5, pp. 605–616, 2022.
- [45] Y. Chen, B. Fang, H. Li, L. Huang, and J. Luo, “Ultrafast online clutter filtering for ultrasound microvascular imaging,” *IEEE Transactions on Medical Imaging*, vol. 44, no. 6, pp. 2477–2491, 2025.
- [46] M. Amin Naji, I. Taghavi, E. Vilain Thomsen, N. Bent Larsen, and J. Arendt Jensen, “Underestimation of flow velocity in 2-d super-resolution ultrasound imaging,” *IEEE Transactions on Ultrasonics, Ferroelectrics, and Frequency Control*, vol. 71, no. 12: Breaking the Resolution Barrier in Ultrasound, pp. 1844–1854, 2024.
- [47] M. Lerendegui, K. Riemer, B. Wang, C. Dunsby, and M.-X. Tang, “Bubble flow field: a simulation framework for evaluating ultrasound localization microscopy algorithms,” *arXiv preprint arXiv:2211.00754*, 2022.
- [48] N. Blanken, B. Heiles, A. Kuliesh, M. Versuis, K. Jain, D. Maresca *et al.*, “PROTEUS: a physically realistic contrast-enhanced ultrasound simulator—part I: numerical methods,” *IEEE Trans. Ultrason. Ferroelectr. Freq. Control*, pp. 1–1, 2024.
- [49] N. Blanken, J. M. Wolterink, H. Delingette, C. Brune, M. Versluis, and G. P. R. Lajoinie, “Super-resolved microbubble localization in single-channel ultrasound rf signals using deep learning,” *IEEE Trans. Med. Imag.*, vol. 41, pp. 2532–2542, 2022.
- [50] H. Belgharbi, J. Porée, R. R. Damseh, V. Perrot, L. Milecki, P. Delafontaine-Martel *et al.*, “An anatomically realistic simulation framework for 3d ultrasound localization microscopy,” *IEEE open j. Ultrason. Ferroelectr. Freq. Control*, vol. 3, pp. 1–13, 2023.
- [51] M. Lerendegui, K. Riemer, B. Wang, C. Dunsby, and M.-X. Tang, “Bubble flow field: a simulation framework for evaluating ultrasound localization microscopy algorithms,” 2022. [Online]. Available: <https://arxiv.org/abs/2211.00754>